Physica Scripta

PAPER

Influence of Fe_2O_3@reduced graphene oxide nanocomposite on the structural, morphological, and optical features of the polyvinyl alcohol films for optoelectronic applications

RECEIVED
1 February 2023

REVISED
26 March 2023

ACCEPTED FOR PUBLICATION
6 April 2023

PUBLISHED
17 April 2023

R M Ahmed[1], T S Soliman[2,3,*], S A Vshivkov[2] and A Khalid[4]

[1] Physics Department, Faculty of Science, Zagazig University 44519, Zagazig, Egypt
[2] Institute of Natural Sciences and Mathematics, Ural Federal University, Ekaterinburg 620000, Russia
[3] Physics Department, Faculty of Science, Benha University, Benha 13518, Egypt
[4] Department of Basic Engineering Sciences, Faculty of Engineering (Shoubra), Benha University, Benha, Egypt
[*] Author to whom any correspondence should be addressed.

E-mail: tarek.attia@fsc.bu.edu.eg

Keywords: polyvinyl alcohol, reduced graphene oxide, refractive index, linear and nonlinear optical parameters

Abstract

Polyvinyl alcohol (PVA) films doped with Fe_2O_3-reduced graphene oxide (rGO) nanoparticles (NPs) were prepared using a casting-method. Fe_2O_3 NPs were synthesized via the hydrothermal process, and then Fe_2O_3 NPs were decorated on the graphene oxide (GO) sheets, where the GO was transferred to rGO during the sonication process. The obtained films were characterized using XRD and FTIR techniques. Optical absorption and transmission data were recorded via a UV–visible spectrophotometer and used to estimate various optical parameters. Increasing the amount of doped Fe_2O_3-rGO NPs in PVA decreased the ability of the prepared nanocomposites to allow visible light to pass through them. Solar material protection factor (SMPF) of PVA (11.93%) improved to 99.3%, corresponding to 2 wt% of Fe_2O_3-rGO NPs doped in the host matrix. The calculated values of the average refractive index are 2.18, 2.25, 2.36, 2.46, and 2.58, corresponding to 0 wt%, 0.5 wt%, 1 wt%, 1.5 wt%, and 2 wt% of Fe_2O_3-rGO NPs doped in PVA. Therefore, the average refractive index showed a dependence on Fe_2O_3-rGO NPs. Low energy region ($E < 2.4$ eV) showed dielectric relaxation time-energy dependent behavior, whereas the high energy region ($E > 2.4$ eV) displayed dielectric relaxation time- energy independent behavior. Increasing the content of the doped NPs in PVA resulted in lowering the surface and volume energy loss.

1. Introduction

Polymer nanocomposite materials have evolved into a vital component of technological advancement and are now an integral part of daily life [1–3]. Nowadays most studies focus on the fabrication of innovative polymer nanocomposite materials with enhanced physical properties. Polymer materials have attracted scientifical and industrial interest due to their low cost, biodegradability, easy synthesis, and good optoelectrical properties [4]. These materials are also promising alternative materials for inorganic semiconductors in optoelectronic applications like; photovoltaic cells, Supercapacitors, magneto-optic data storages, gas sensors, and biomedical applications [4–7]. Several works have been done to enhance the performance of the optical properties of the polymer material via incorporating various filler materials with different concentrations and/or different sizes [8]. Optical parameters such as absorbance, reflection, transmission, absorption coefficient, optical band gap, Urbach energy, refractive index, extinction coefficient, optical dielectric constant, optical dielectric loss, and optical conductivity are the key factor to evaluate the material's suitability as a suitable candidate for the optoelectronic applications, which can be enhanced and tuned via the changing of the filler nature, size, and its distribution in a polymer matrix.

Polyvinyl alcohol (PVA) is a biocompatible and thermostable polymer material [9]. It has been used as a host matrix for various filler materials, owing to their good features like; non-corrosive nature, soluble in water, thermal stability, good film forming, and highly transparent film. In our previous work, different nanoparticles (NPs) like SiO_2 [10], ZnO [11], $Cd_{0.5}Zn_{0.5}Fe_2O_4$ [12], La_2ZnO_x [13], and Mn_2O_3-rGO [14] have been used as filler materials in PVA polymer matrices to tune and enhance optical properties and to tailor their optical parameters for optical industrial applications.

Badawi *et al* [15] studied the effect of reinforcing different concentrations of Fe_2O_3 nanoparticles on the structural and optical properties of the PVA/graphene (G) blend. It was found that the addition of Fe_2O_3 NPs to the blend matrix causes a decrease in the optical band gap and an enhancement in the optical dispersion parameters. Also, Badawi *et al* [16] studied the effect of reinforcing 2 wt% from Fe_2O_3, Pb_2O_3, and MnO_2 on the structural and optical properties of PVA/rGO blend films. The obtained results revealed that Fe_2O_3 has more effect on the decrease in the optical band gap than Pb_2O_3, and MnO_2. Aslam *et al* [17] reported an improvement in the optical absorption of the PVA polymer films when reinforced with GO sheets. Recently, researchers have succeeded to decorate various nanoparticles on reduced graphene (rGO) sheets to enhance their performance [18–26]. Previously, our team succeeded in fabricating Mn_2O_3-rGO composite which was used as a filler material in the PVA matrix [14].

As mentioned earlier [15, 16], two blends of polymers, PVA/G and PVA/rGO, have been prepared and then reinforced with different concentrations of Fe2O3 NPs and different nanoparticle types, respectively. Herein, the Fe_2O_3 NPs were firstly synthesized via the hydrothermal process and then the obtained sample was decorated on the graphene oxide (GO) sheets. Moreover, the GO was transferred to rGO during the sonication process which is in good accordance with the literature [19]. Then, the obtained composite, Fe_2O_3-rGO, was reinforced in the host matrix, PVA, with different concentrations. This study intends to investigate the linear and nonlinear optical parameters of PVA films reinforced with different concentrations of Fe_2O_3-rGO nanoparticles. The x-ray diffractometer (XRD), Fourier transfer infrared (FTIR), and UV–visible techniques were used to study the structure and optical properties of the prepared polymer films, respectively. This study provides reporting data about the enhancement of their performance in optoelectronic applications.

2. Experimental and methods

2.1. Materials

Polyvinyl alcohol (PVA), with a molecular wight $= 1 \times 10^6$, was purchased from Qualikem Company. Fe_2O_3-rGO NPs were prepared by the co-precipitation method. 1 M $FeCl_3$ in 100 ml deionized water (DIW) was heated to 80 °C, and ammonia was added to the solution with continuous stirring for 2 h. Then, the product was centrifuged (8000 rpm), and the precipitated particles were collected and washed with DIW. The prepared Fe_2O_3 NPs were dried for 24 h. (at 80 °C), followed by calcination for 4 h (at 400 °C). Finally, the prepared Fe_2O_3 NPs were decorated on GO by mixing them in 100 ml DIW and sonicating them for 15 min (GO transferred to rGO during the sonication process [14]).

2.2. Preparation of Fe_2O_3-rGO-PVA nanocomposite films

Firstly, 5 gm of PVA powder was dissolved in 100 ml distilled water at 70 °C, with the help of magnetic stirrer. Then, different concentrations of Fe_2O_3-rGO NPs were added to the host matrix and distributed via the probe ultrasonic process. The sonication continued for 5 min. Then the solution was kept in a vacuum chamber for an hour to remove any bubbles produced during the sonication process. Finally, the solution was cast in glass petri-dishes and lifted to dry at room temperature and dry atmosphere for a week. The obtained polymer films were kept in a vacuum chamber for a night to remove any residual solvents form the polymer films. The polymer film thickness was measured using a digital micrometer and was found to be about 100 μm. The chemical structure and schematic synthesis of Fe_2O_3-rGO nanocomposite and Fe_2O_3-rGO-PVA film is shown in scheme 1.

2.3. Characterization and setups

The x-ray diffraction pattern of the Fe_2O_3-rGO-PVA films was investigated through Bruker D8 diffractometer, Cu-Kα radiation $\lambda = 1.5418$ Å. Fourier transform infrared (FTIR, Vertex 70-Bruker-Germany) spectrometer was used with range (4000 to 400 cm^{-1}, 4 cm^{-1} resolution). The Fe_2O_3-rGO-PVA films morphology was investigated using OLYMPUS-BX51optical microscope and Carl-Zeiss LEO982 scanning electron microscope (SEM). The UV-visible absorption and transmission spectra were collected via Cary5000-UV spectrophotometer.

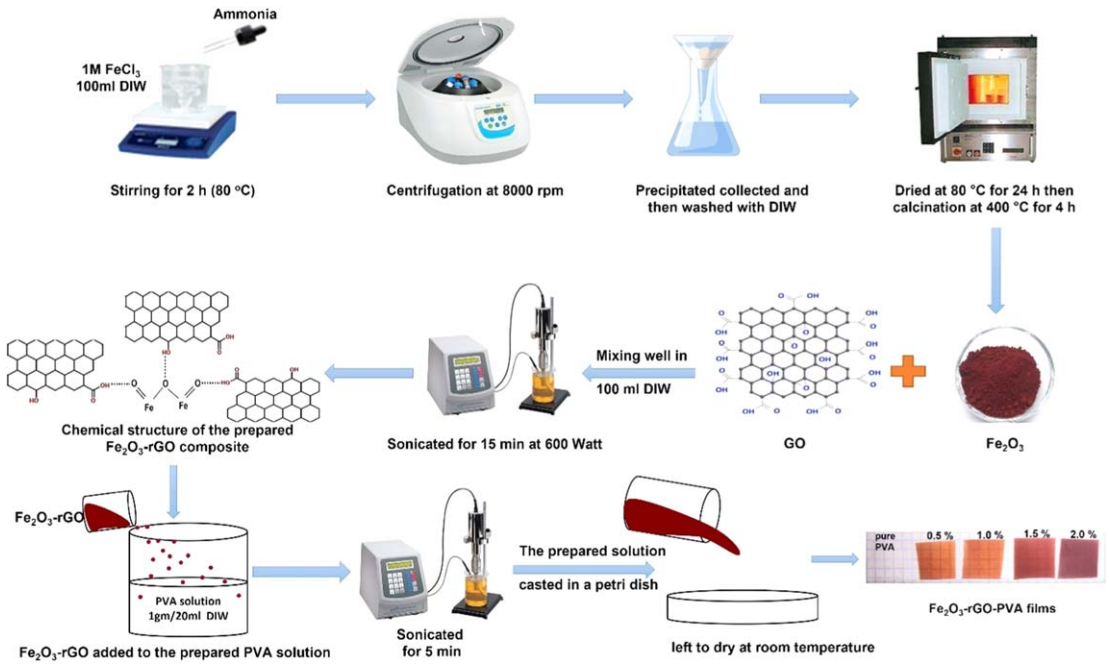

Scheme 1. The schematic synthesis of Fe_2O_3-rGO nanocomposite and Fe_2O_3-rGO-PVA films.

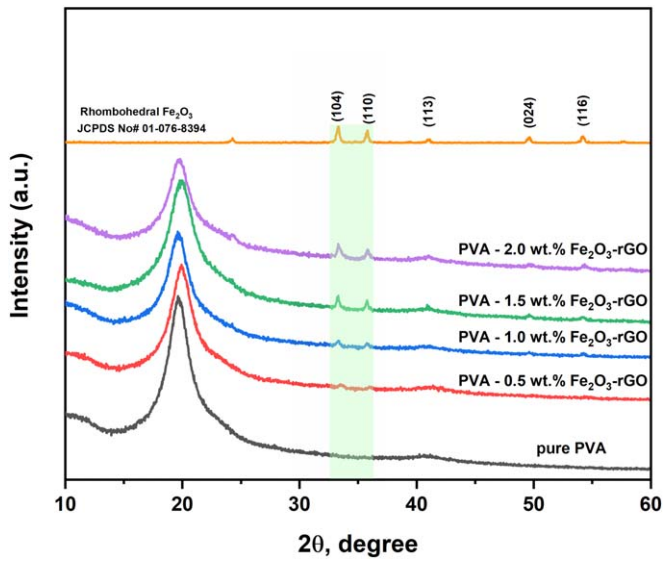

Figure 1. XRD patterns for Fe_2O_3-rGO-PVA composite films.

3. Results and discussions

3.1. XRD analysis

Figure 1 shows the XRD pattern of the pristine sample and the pristine reinforced with different concentrations of Fe_2O_3-rGO NPs. The well-known broad hump at 19.62° is indexed to the (101) diffraction plane of the characteristic peak of semicrystalline PVA film.

With the addition of Fe_2O_3-rGO NPs to the PVA matrix, the hump descends and broadened gradually with increasing the NPs concentration. In addition, the peaks at 33.3° and 35.8°, indexed to the rhombohedral Fe_2O_3 NPs (JCPDS No.# 01–076–8394), observed, and became more pronounced at higher Fe_2O_3 NPs concentration. This reveals the increase in PVA film amorphousity with the addition of the Fe_2O_3-rGO NPs to the matrix [27, 28]. In addition, the Fe_2O_3 peaks at higher concentration became more pronounced and vanishes of it at lower concentration is an indication of the increase of the particle size because of the agglomeration with rising

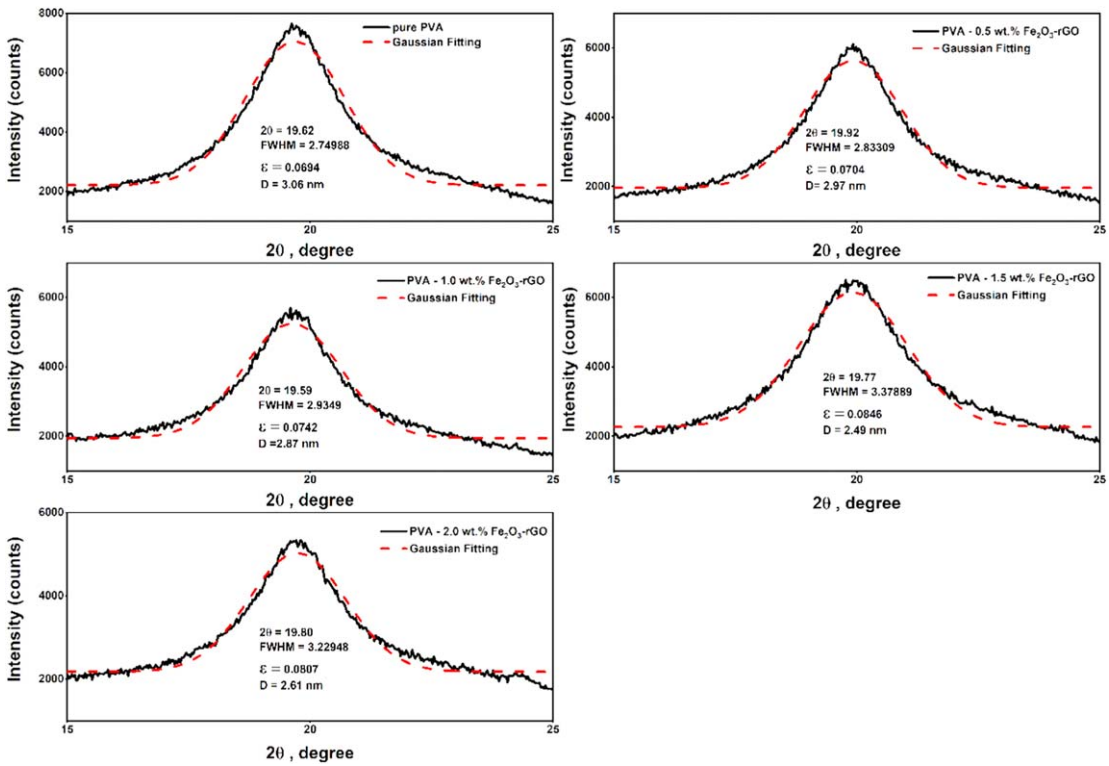

Figure 2. Gaussian fitting of (101) peak for Fe_2O_3-rGO-PVA composite films.

Table 1. Geometrical parameters of Fe_2O_3-rGO-PVA composite films.

Sample	FWHM (degree)	2θ, degree	D (nm)	ε	δ (nm^{-2})
Pure PVA	2.74	19.62	3.06	0.069	0.107
0.5%	2.83	19.92	2.97	0.070	0.113
1.0%	2.93	19.59	2.87	0.074	0.121
1.5%	3.38	19.77	2.49	0.085	0.161
2.0%	3.23	19.80	2.61	0.081	0.147

of Fe_2O_3-rGO NPs concentration. Furthermore, the H-bonds formed between the Fe_2O_3-rGO NPs and the hydroxyl groups of PVA molecules. Recently, Badawi *et al* [15] concluded that the addition of Fe_2O_3 to the PVA/graphene decreases the PVA semi-crystallinity.

Gaussian fitting of the characteristic peak (101) of PVA films was used to estimate the crystallite size (D), the internal strain (ε), and dislocation density (δ), as shown in figure 2. This can be calculated by the following equations [14],

$$D = \frac{0.9\ \lambda}{\beta\ \cos\ \theta} \tag{1}$$

$$\varepsilon = \frac{\beta}{4\ \tan} \tag{2}$$

$$\delta = \frac{1}{D^2} \tag{3}$$

where β is the full width at half maximum (FWHM) and θ is the Bragg's angle. The obtained data are presented in table 1 and shown in figure 2.

Obviously, as the Fe_2O_3-rGO NPs concentration in the PVA matrix increases the D value decreases. This is caused due to the incorporation of the Fe_2O_3-rGO NPs into the PVA matrix causing a decrement in the hydrogen bonding in the PVA matrix and forming of hydrogen bonding between the Fe_2O_3-rGO NPs and the PVA molecules [29–31]. In contrary, the ε and δ values are found to increase with the increase in the Fe_2O_3-rGO concentration. The high values of ε and δ confirms the decrease in polymer films crystallinity [27, 32].

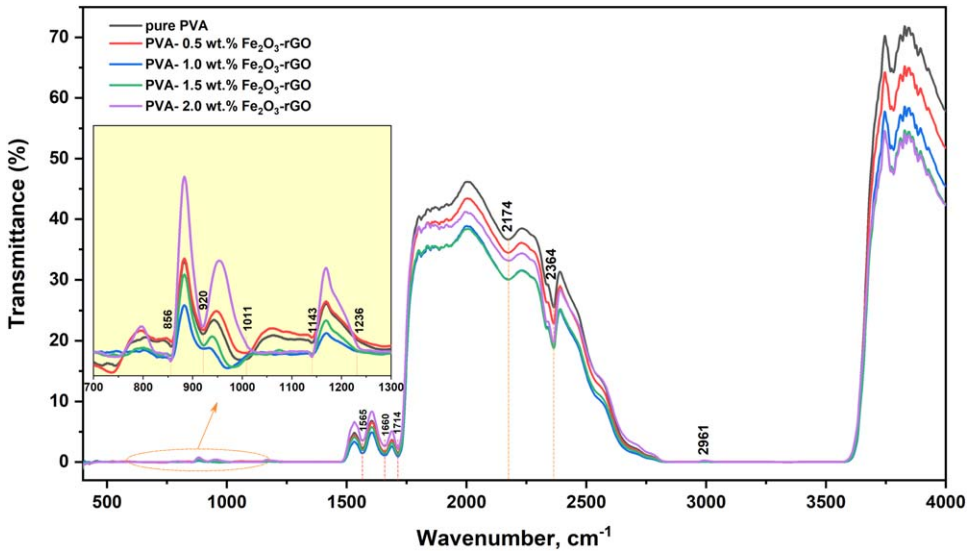

Figure 3. FTIR spectra for Fe_2O_3-rGO-PVA composite films.

3.2. FTIR and optical microscope analysis

Figure 3 shows the FTIR spectra of Fe_2O_3-rGO-PVA films. It shows a broad band at 3000–3600 cm^{-1} which is assigned to O–H stretching vibration mode of PVA molecules. The absorption band at 2961 cm^{-1} is related to C-H asymmetric stretching mode. Furthermore, the bands 1714, 1660, 1565 cm^{-1} are representing the C = O vibrational stretching, C = C stretching vibration, and (O–H&C–H) bending modes, respectively [33–35]. 1143 cm^{-1} related to the C-O-C vibrational stretching mode of acetyl group in PVA matrix, and 1236 cm^{-1} related to $-CH_2$ wagging. While the bands at 856, 1011 cm^{-1} are related to the C–H rocking vibrations and C–O stretching of acetyl groups, respectively. The band at 920 cm^{-1} is related to the epoxides in GO [31]. The bands intensity was changed with the addition of Fe_2O_3-rGO NPs in the PVA matrix which may be caused by the formation of the hydrogen bonds between the Fe_2O_3-rGO NPs and the PVA molecules [13]. In addition, the incorporation of Fe_2O_3-GO NPs in the PVA matrix causes a decrement in the hydrogen bonds between the PVA molecules and produces hydrogen bonds between Fe_2O_3-GO NPs and PVA molecules [31]. The band position was slightly changed as in the band at 856 cm-1 for pure PVA shifted to lower value at 854 cm^{-1} for 2 wt% Fe_2O_3-rGO-PVA film. This slight shift is an indication of the formation of hydrogen bonds [36].

The morphological study of the polymer films surface was investigated using the optical microscope. In figure 4 a smooth surface was observed in the bright field image of the pure PVA. With the addition of Fe_2O_3-rGO NPs in the PVA matrix, particles, small spherical, and big irregular shapes were seen in the polymer films. The big particles represent clusters of Fe_2O_3-rGO NPs, which formed due to aggregations caused by the magnetic inductions between the Fe_2O_3-rGO NPs each other. This aggregation increases with increasing the Fe_2O_3-rGO NPs concentrations in the PVA matrix. Figures 4(f)–(g) shows the surface morphology of PVA films doped with Fe_2O_3-rGO NPs. PVA films look rough, and the white spots represent the embedded Fe_2O_3-rGO NPs. In addition, these NPs grow in size and are denser at 2.0 wt% (figure 4(g)) as compared with 0.5 wt% (figure 4(f)). It is clear from the histogram shown in figure 4(h) that the minimum and maximum particle sizes are about 44 and 413 nm for PVA-0.5 wt% Fe_2O_3-rGO film and about 60 and 456 nm for PVA-2.0 wt% Fe_2O_3-rGO film, respectively. The growth in the crystallite size was caused due to the aggregations, which are in good accordance with the XRD data.

3.3. Optical properties

3.3.1. Skin depth, interband transitions, and urbach energy

UV-vis spectrometer was used to measure the transmission and absorption of the nanocomposites of Fe_2O_3-rGO-PVA in a range of wavelengths from 200 nm to 1000 nm, as seen in figures 5(a), (b), respectively. The host matrix (PVA) has a transmission value of 89% at 400 nm, which decreased to 11%, 3%, 0.9% and 0.4%, corresponding to the added amount of Fe_2O_3-rGO NPs of 0.5 wt%, 1 wt%, 1.5 wt%, and 2 wt%, respectively. Therefore, increasing the doped content of Fe_2O_3-rGO NPs in the host matrix caused an obvious decrease in the transmission due to acting these NPs as scattering centers, in satisfactory accordance with the relevant literature [37].

Plotting absorption of nanocomposite divided by the absorption of PVA versus wavelength, as seen in figure 5(c) illustrated an obvious absorption peak in the visible region ($\lambda > 400$ nm), which was not clear in the

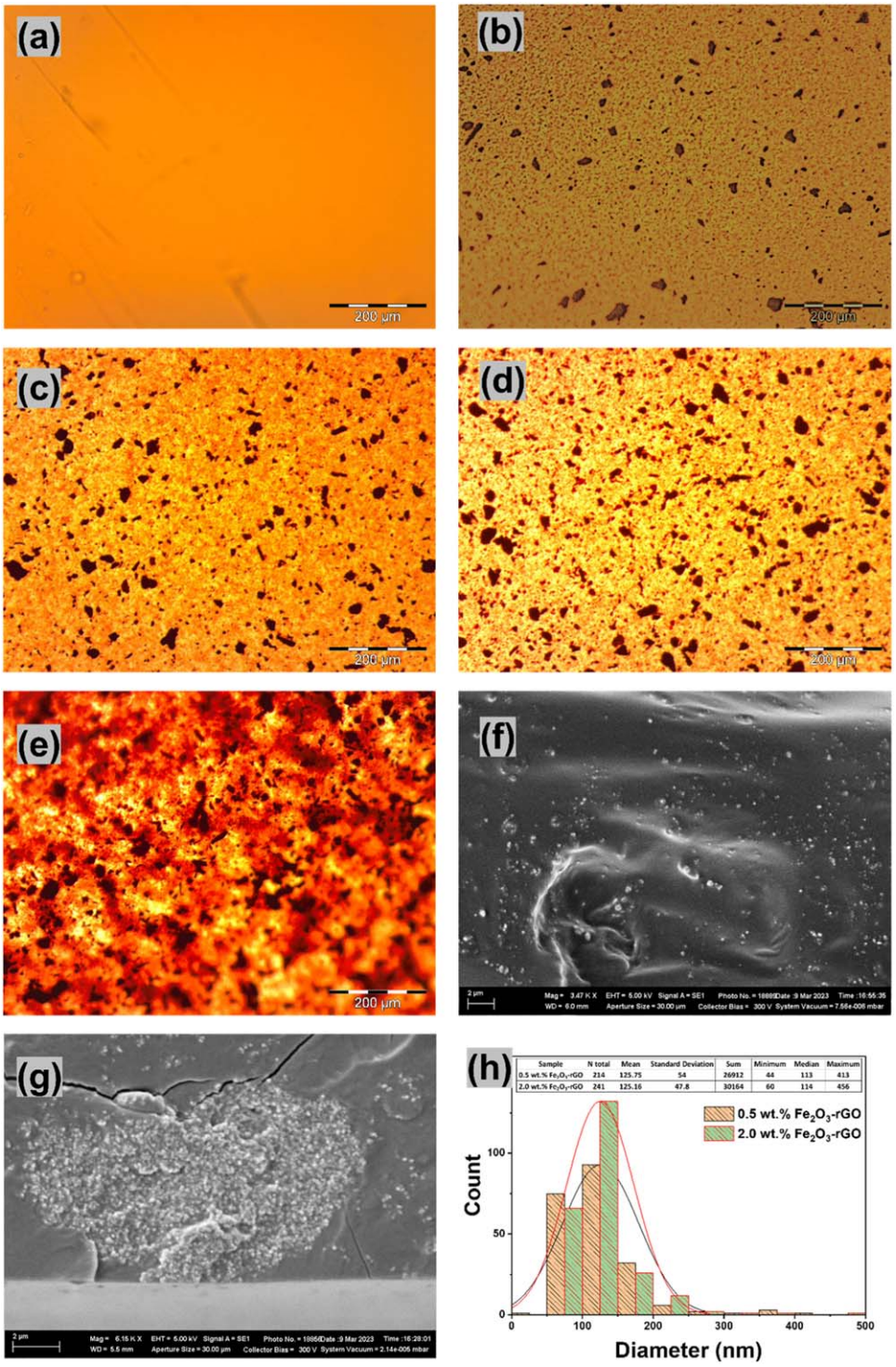

Figure 4. Optical microscope images (a-e), SEM images (f-g), and the histogram (h) of PVA- Fe_2O_3-rGO films. (a) 0, (b) & (f) 0.5, (c) 1.0, (d) 1.5, and (e) & (g) 2.0 wt% Fe_2O_3-rGO.

absorption spectra of each nanocomposite, see figure 5(b). The positions of the observed peaks in figure 5(c) are at wavelengths of 425 nm, 423 nm, 421 nm, and 416 nm corresponding to the doped amounts of Fe_2O_3-rGO of 0.5 wt%, 1 wt%, 1.5 wt%, and 2 wt%, respectively. The clear peaks in figure 5(c) correspond to Fe_2O_3 NP_S, in good agreement with a published work [38].

The distance that an electromagnetic wave is able to go into a polymeric substance is referred to as the skin depth (δ) [39]. The value of the skin depth can be calculated by taking the reciprocal of the absorption coefficient (α), which represents the ratio of the absorption to the sample thickness). For the different nanocomposites of Fe_2O_3-rGO-PVA, the dependence of the skin depth (δ) on wavelength is depicted in figure 5(d). Increasing the content of the Fe_2O_3-rGO NPs in the host matrix of PVA resulted in a decrease in the skin depth of the

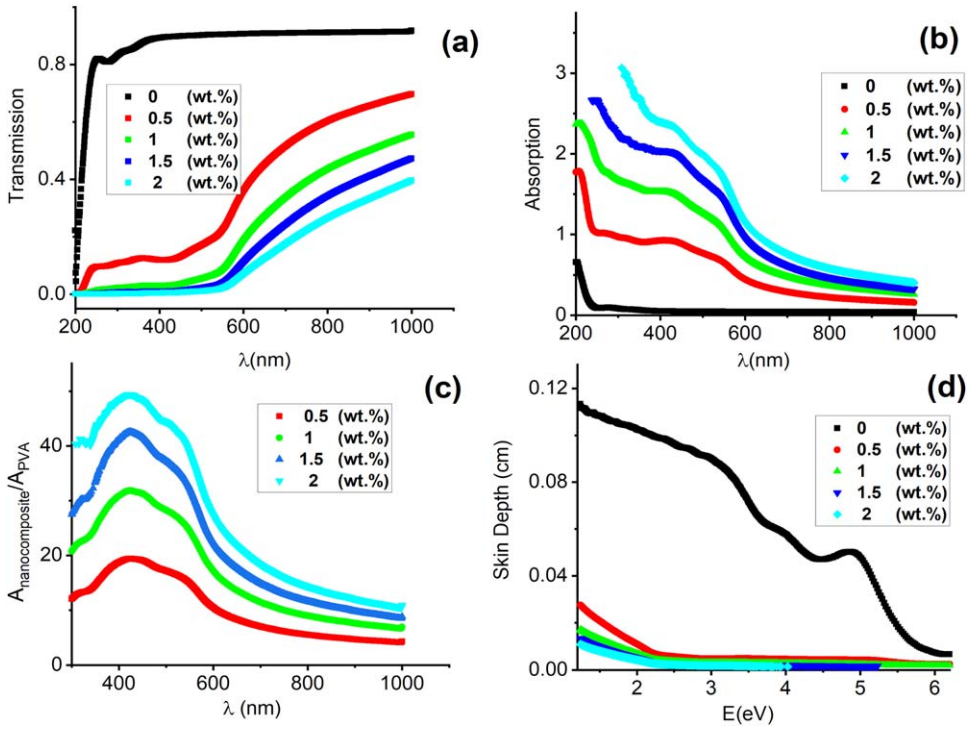

Figure 5. The dependence of (a) transmission (%) (b), absorption, and (c) $A_{nanocomposite}/A_{hosting\ blend}$, on the incident wavelength, for the different concentrations of Fe_2O_3-rGO doped in PVA. (d) The dependence of skin depth on energy (E) for the different concentrations of Fe_2O_3-rGO doped in PVA.

nanocomposites. This behavior can be attributed to increasing the absorption and decreasing the transparency by increasing the NPs content.

The absorption spectrum fitting (ASF) method was successfully used to estimate the optical band gap based on the absorption spectra according to the following relation [40, 41]:

$$\alpha(\lambda) = Z(hc)^{-1+m}\,\lambda(\lambda^{-1} - \lambda_g^{-1})^m \tag{4}$$

Where α is the absorption coefficient, h is Plank's constant, Z is a constant, c is the light speed, and λ_g represents the wavelength where the optical gap occurs. The index 'm' defines the kind of electronic transitions responsible for the absorption process. The values of m can be 1/3 and 3 correspond to direct and indirect forbidden transitions, respectively, whereas the values of 0.5 and 2 are related to the direct and indirect allowed transitions, respectively. The best fit was achieved for m = 0.5, implying that direct allowed transition was demonstrated for all samples. The value of λ_g^{-1} shown in figure 6(a) was obtained by extrapolating the linear portion of the plot of $(A\lambda^{-1})^{1/m}$ against λ^{-1} at the zero value of $(A\lambda^{-1})^{1/m}$. The values of ASF optical gap (E_{gab}^{ASF}) were calculated by the product of 1239.83 times λ_g^{-1} and listed in table 2 for all of the samples under investigation.

The optical gap energies were also calculated using Tauc's formula, which was derived from the dependence of the absorption coefficient on the photon energy as follows [38, 39]:

$$\alpha E = B(E - E_{gab}^{Tauc})^m \tag{5}$$

where B is a constant that depends on the transition probability, E_{gab}^{Tauc} is the Tauc band gap energy, E is the photon energy (eV), and m expresses the nature of the electronic transition. The dependence of $(aE)^{1/m}$ on the photon energy for the different nanocomposites is illustrated in figure 6(b). The intercept on the energy axis of the best linear fit of the data in figure 6(b), for m = 0.5, was used to derive the values of E_{gab}^{Tauc}. Table 2 reported the values of E_{gab}^{Tauc} for all the investigated samples which were obtained from the direct allowed transition.

The values of E_{gab}^{Tauc} are 5.956 eV, 5.061 eV, 4.298 eV, 3.694 eV, and 3.076 eV, whereas E_{gab}^{ASF} has values of 5.579 eV, 5.083 eV, 4.091 eV, 3.472 eV, and 3.099 eV, corresponding to 0 wt%, 0.5 wt%, 1 wt%, 1.5 wt%, and 2 wt% of Fe_2O_3-rGO NPs doped in PVA. There is a similarity between the two methodologies used to calculate the optical gap energy of nanocomposites of Fe_2O_3-rGO-PVA.

The energy gap of bulk Fe_2O_3 (2.1 eV) [42] is less than the energy gap of the prepared Fe_2O_3 NPs only (3.67 eV) or Fe_2O_3-rGO NPs only (4.08 eV), as deduced in previous work [43]. This result is due to the influence of quantum confinement in agreement with the literature [43]. In addition, increasing the content of the doped Fe_2O_3-rGO NPs in PVA resulted in decreasing the optical gap energy of the host matrix. This result can be due to

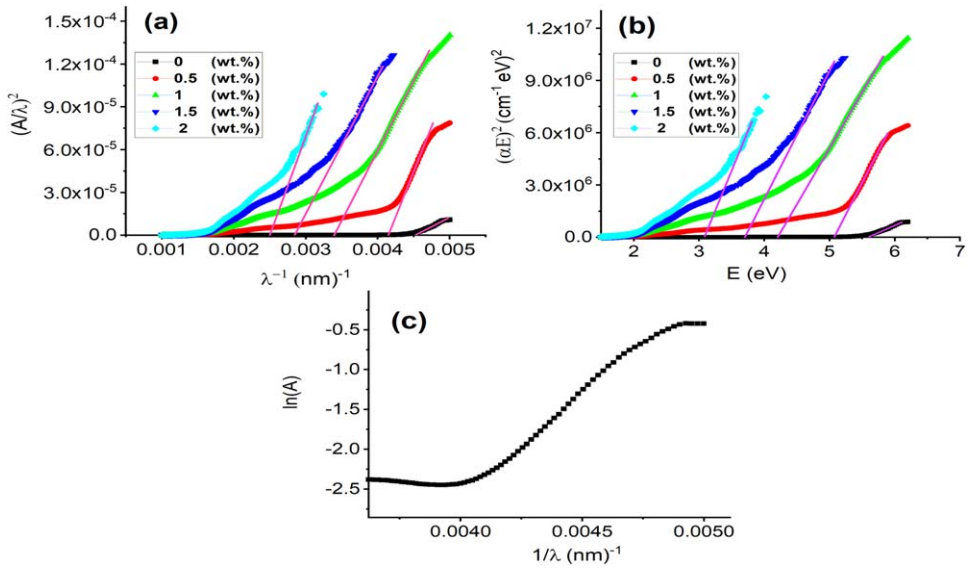

Figure 6. For the different concentrations of Fe_2O_3-rGO doped in PVA, the variation of (a) $(A/\lambda)^2$ versus $(1/\lambda)$, and (b) $(\alpha E)^2$ versus E. (c) the variation of ln(A) versus $(1/\lambda)$ for pure PVA.

the increase in the size of Fe_2O_3-rGO NPs due to aggregation and the modification in the structure of PVA by the added NPs [44, 45]. This finding is in good agreement with XRD and SEM results. Additionally, as stated in the literature [37], reducing the gap energy by adding more NPs indicates that the Fe_2O_3-rGO-PVA nanocomposites are becoming more semiconducting in nature.

Urbach's law [46], which relates the absorption coefficient to the incident photon energy, was successfully revised in the ASF model, leading to the following modified formula [47]:

$$A(\lambda) = Pexp\left(\frac{hc\lambda^{-1}}{E_{Tail}}\right) \tag{6}$$

Where P is a constant, and E_{Tail} is the width of the tail of localized states (Urbach energy), when an optical transition occurs between a localized tail state near the valence band and an extended conduction band state above the mobility edge. The inverse of the slope, generated by the best linear fit of the lnA - λ^{-1} plot, was multiplied with 1239.83 to determine E_{Tail}. The dependence of lnA on λ^{-1} is shown in figure 6(c) for PVA, as an example for all the examined samples. As shown in table 2, increasing the content of Fe_2O_3-rGO NPs doped in PVA resulted in increasing E_{Tail} of PVA from 0.465 eV to be 0.820 eV for the highest content (2 wt%). Consequently, the defects increased in the nanocomposites by increasing the content of the doped NPs. As displayed in table 2, the values of E_{Tail}, for all the studied samples, illustrate an opposite behavior of the optical gaps [(E_{gab}^{ASF}) and (E_{gab}^{Tauc})]. Table 2 contains a comparison between the optical gap energy and Urbach energy acquired from various earlier publications [37–39, 48–50] and the results of the current investigation.

The strength of electron-phonon ($E_{e\text{-}ph}$) interactions is termed by the steepness parameter (S) ($E_{e\text{-}ph} = 2/3S$ [51]), which causes a broadening of the absorbance edge:

$$S = \frac{T_{room}\, k_B}{E_{Tail}} \tag{7}$$

where k_B is the Boltzmann constant, and T_{room} is the room temperature in Kelvin. $E_{e\text{-}ph}$ rose from 11.90 for PVA to 20.94 for 2 wt% of the doped Fe_2O_3-rGO NPs in PVA, as shown in table 2. This behavior can be a result of increasing the filled bands by increasing the added amounts of the doped Fe_2O_3-rGO NPs [52].

Obtaining the number of carbon atoms per molecule based on the values of the calculated energy of the optical gap (E_{gab}^{Tauc}), was proposed by Fink *et al* [53] using the following relation:

$$E_{gap}^{Tauc} = \frac{34.3}{\sqrt{N}} \tag{8}$$

where N is the number of carbon atoms in the carbonaceous cluster. Table 2 shows that the values of N are 38, 46, 64, 86, and 124, corresponding to 0 wt%, 0.5 wt%, 1 wt% 1.5, wt%, and 2 wt%. of Fe_2O_3-rGO NPs doped in PVA. Therefore, increasing the added amount of the doped Fe_2O_3-rGO NPs can increase the conjugation in the monomer unit of the host matrix. This result agrees well with a previously published work [54].

Table 2. Tauc optical gap ($\mathbf{E_{gab}^{Tauc}}$), ASF optical gap ($\mathbf{E_{gab}^{ASF}}$), tailing state energy (E_{Tail}), the steepness parameter (S), the strength of electron-phonon interactions ($E_{e\text{-}ph}$), carbon atoms per conjugated length (N), solar material protection factor (SMPF), and visible solar transmittance (T_{vis}).

	Current Work Content of Fe_2O_3-rGO (wt%) doped in PVA					Previously published works				
						PVA [48]	0.5 & 1wt% of Fe_2O_3 doped in PVA/PEG [37]	1 wt% & 5 wt% of Fe_2O_3 NPs doped in chitosan [38]	0% & 0.012% (w/w) of rGO doped in PVA [49]	0% & 2% of rGO doped in PVA [50]
Optical Parameter	0	0.5	1	1.5	2					
$\mathbf{E_{direct}^{ASF}}$ (eV)	5.579	5.083	4.091	3.472	3.099					
$\mathbf{E_{direct}^{Tauc}}$ (eV)	5.595	5.061	4.298	3.694	3.076	5.31	5.15 & 4.83	3.14–2.80	5.29 & 3.59	3.57 & 2.72
$\mathbf{E_{Tail}}$ (eV)	0.465	0.740	0.762	0.809	0.820	0.20	1.10 & 1.95		0.20 & 0.85	
$Sx10^{-2}$	5.599	3.524	3.426	3.223	3.183					
$E_{e\text{-}ph}$	11.90	18.92	19.42	20.68	20.94					
N	38	46	64	86	124					
T_{vis} (%)	90.4	25.9	11.4	6.15	3.64					
SMPF (%)	11.3	85.9	95.9	98.5	99.3					

3.3.2. Solar protection factors

3.3.2.1. Visible solar transmittance (T_{vis})

The visible solar transmittance (T_{vis}) gives an indication of the solar energy transmittance. As inferred by the following equation, calculating T_{vis} can provide valuable information regarding the skin's degree of protection:

$$T_{vis} = 1 - \frac{\sum_{\lambda=380\ \mathrm{nm}}^{\lambda=780\ \mathrm{nm}} \Delta\lambda\ T_\lambda D_\lambda V(\lambda)}{\sum_{\lambda=380\ \mathrm{nm}}^{\lambda=780\ \mathrm{nm}} \Delta\lambda\ D_\lambda V(\lambda)} \tag{9}$$

where $D\lambda$ is the relative spectral distribution of illuminant D65 [55, 56], $T(\lambda)$ is the spectral transmittance of the studied nanocomposites obtained from figure 5(a), λ is the wavelength, $\Delta\lambda$ is the wavelength interval ($\Delta\lambda = 10$ in a range of wavelengths from 380 nm to 780 nm), and $\Delta\lambda\ D_\lambda V(\lambda)$ are extracted from published literature [57], and $V(\lambda)$ is the luminous spectral efficiency for photonic vision provided by the standard observer for photometry [56, 58]. The high transmission of visible light through the studied samples was detected in the host matrix of PVA, which has the highest T_{vis} (90.4%), as reported in table 2. Table 2 shows that increasing the amount of doped Fe_2O_3-rGO NPs in PVA decreased the ability of the prepared nanocomposites to allow visible light to pass through them. The value of T_{vis} given by 2 wt% of Fe_2O_3-rGO NPs doped in PVA was the lowest possible value (3.64%).

3.3.2.2. Solar material protection factor (SMPF)

The solar material protection factor (SMPF) is a measure of the resistance of PVA and its nanocomposites against deterioration caused by Sunlight. SMPF was calculated from the following formula [57]:

$$SMPF = 1 - \frac{\sum_{\lambda=300\ \mathrm{nm}}^{\lambda=600\ \mathrm{nm}} C_\lambda S_\lambda \Delta\lambda T(\lambda)}{\sum_{\lambda=300\ \mathrm{nm}}^{\lambda=600\ \mathrm{nm}} C_\lambda S_\lambda \Delta\lambda} \tag{10}$$

Where $T(\lambda)$ is the spectral transmittance of the studied samples obtained from figure 5(a), $S\lambda$ is the relative spectral distribution of Sunlight [56, 59], $C\lambda = \exp(-0.012\lambda)$, $C_\lambda S_\lambda \Delta\lambda$ are obtained from a published reference [57], and $\Delta\lambda$ is the wavelength interval ($\Delta\lambda = 5$ in a range of 300 nm − 400 nm and $\Delta\lambda = 10$ in a range of 400 nm–600 nm). The tabulated values of SMPF, for all the samples under study in table 2, show that SMPF of PVA (11.93%) improved to 99.3%, corresponding to 2 wt% of Fe_2O_3-rGO NPs doped in the host matrix.

3.3.3. Refractive Index (n) and attenuation coefficient (k)

One of the most interesting things about polymeric materials is that their refractive index has a strong relationship with the local electric field and the ability of the electrons inside the material to be polarized. Additionally, the dispersion behavior of the refractive index has an impact on the design of optical communication systems as well as a wide variety of optical instruments. The refractive index was calculated using Fresnel's law as follows [44, 60]:

$$n = \left(\frac{1+R}{1-R}\right) + \sqrt{\frac{4R}{(1-R)^2} - k^2} \tag{11}$$

Where R is the reflection which was calculated from the relation of $R = (1 - Transmission \times \exp(Absorption)^{0.5}$ [5], and k is the extinction coefficient that depends on the absorption coefficient (α) and the incident wavelength (λ), according to the relation of $k = \frac{\alpha\lambda}{4\pi}$ [61]. The dependence of the extinction coefficient (k) on wavelength for all samples is plotted in figure 7(a). Increasing the content of Fe_2O_3-rGO NPs in PVA enhanced the values of the extinction coefficient (k). In addition, increasing the incident wavelength caused an increase in the values of the extinction coefficient (k) of the host matrix (PVA) as shown in the inset of figure 7(a), which is attributed to the interaction between the light and the material of the host matrix. This behavior disappeared upon the addition of the doped Fe_2O_3-rGO NPs in agreement with some published studies [37, 48].

Dispersion curves are observed in figure 7(b), for all the content of Fe_2O_3-rGO NPs in PVA, resulting from the slow decrease of the refractive index (n) with increasing the incident wavelength. However, the refractive index of PVA suffered from a sharp decrease, as seen in the inset of figure 7(b), typically as reported in the literature for PVA [39]. Increasing the refractive index of PVA by increasing the content of the doped Fe_2O_3-rGO NPs in PVA can be attributed to increasing the number of particles in the material of the nanocomposites. Therefore, the interaction between the incident light and a large amount of particles will increase the refraction, and as a result, the nanocomposites of Fe_2O_3-rGO-PVA will have a higher refractivity [62].

Understanding the relationship between the optical bandgap energy (E_g) and the linear refractive index can help researchers understand the band structure of samples and determine more optical parameters. In this study, several models were used to explore the relationship between the energy gap and refractive index, including Moss (n_M) [63], Anani, *et al* ($n_{A,\ et\ al}$) [64], Reddy-Ahammed ($n_{R,\ Ah}$) [65], Ravindra, *et al* ($n_{R,\ et\ al}$) [66],

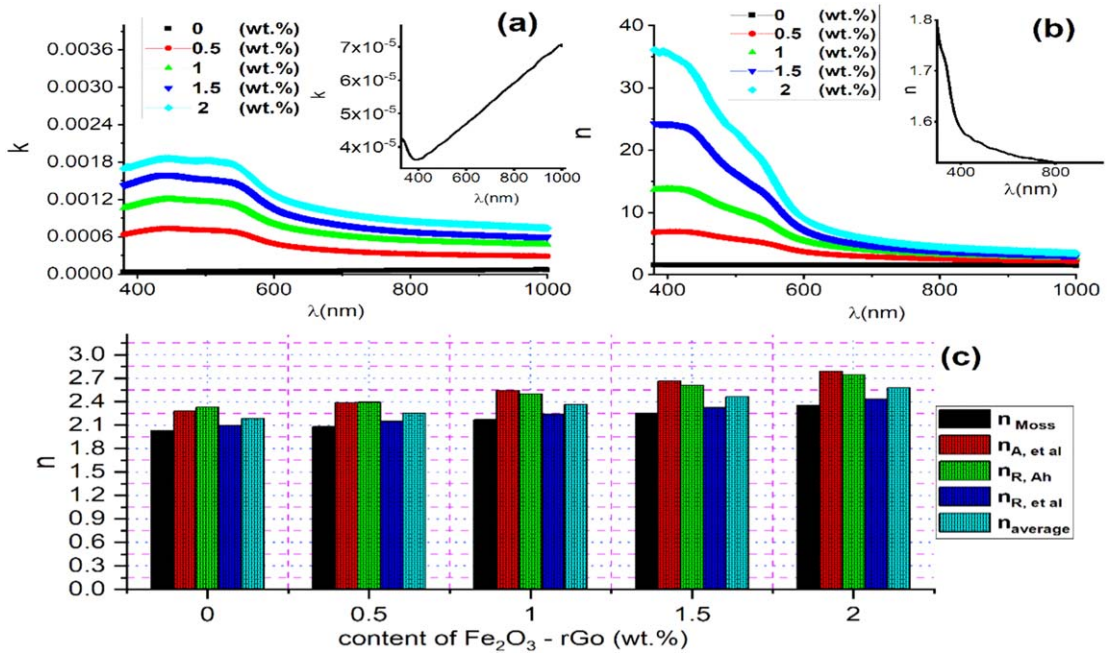

Figure 7. For the different concentrations of Fe_2O_3-rGO doped in PVA, the dependence of (a) attenuation coefficient (k) (the inset belongs to PVA), and (b) refractive index (n) (the inset belongs to PVA) on the incident wavelength. (c) The variation of the refractive index (n) with the content of Fe_2O_3-rGO doped in PVA, for the different theoretical models by using E_{gab}^{Tauc}.

and average refractive index ($n_{average}$):

$$n_M^4 = \frac{95\ (eV)}{E_g} \tag{12}$$

$$n_{A,\ et\ al} = 3.4 - 0.2\ E_g \tag{13}$$

$$n_{R,Ah}^4 = 154(-0.365 + E_g)^{-1} \tag{14}$$

$$n_{R\ et\ al}^4 = \frac{108\ (eV)}{E_g} \tag{15}$$

$$n_{average} = [n_M + n_{A,\ et\ al} + n_{R,\ Ah} + n_{R,\ et\ al}] \div 4 \tag{16}$$

By using the estimated values of $\mathbf{E_{direct}^{Tauc}}$, and these different models (equation (8)–12), the values of the linear refractive index (n) were calculated for all the nanocomposites under study, as displayed in figure 7(c). The various models displayed approximations of the calculated linear refractive index for each sample. The calculated values of the average refractive index ($n_{average}$)are 2.18, 2.25, 2.36, 2.46, and 2.58, corresponding to 0 wt%, 0.5 wt%, 1 wt%, 1.5 wt%, and 2 wt% of Fe_2O_3-rGO NPs doped in PVA. Therefore, the average refractive index ($n_{average}$) showed a dependence on Fe_2O_3-rGO NPs as it increased by increasing the amount of the doped NPs in PVA.

3.3.4. Optical conductivity (σ_{opt})

Determining a material's optical conductivity (σ_{opt}) can help one comprehend the electronic states that the material possesses, according to the following relation [67]:

$$\sigma_{optical} = \frac{cn\alpha}{4\pi} \tag{17}$$

where c is the light velocity, α is the absorption coefficient, n is the refractive index, and λ is the wavelength. An obvious development in the value of optical conductivity (σ_{opt}) of PVA was observed in figure 8(a) by increasing the doped amount of Fe_2O_3-rGO NPs in PVA. Figure 8(a) shows that at $\lambda > 750$ nm, the optical conductivity (σ_{opt}) is wavelength independent. However, increasing the absorption in the region of wavelength less than 750 nm, as seen before in figure 5(b), caused an improvement in the values of σ_{opt} for all studied samples.

3.3.5. Optical dielectric constants

The optical dielectric constant is directly related to the density of states within the band; therefore, it is beneficial for understanding the band structure of tested samples. The summation of the real part (ε_r) and the imaginary

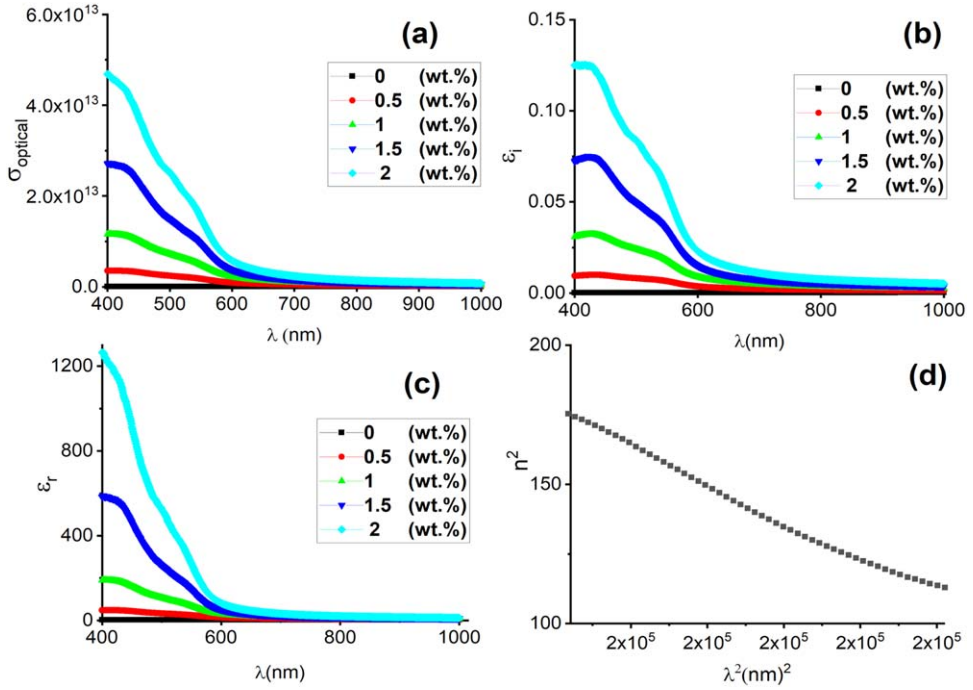

Figure 8. For the different concentrations of Fe_2O_3-rGO doped in PVA, the variation of (a) optical conductivity ($\sigma_{optical}$), (b) real (ε_r), and (c) imaginary (ε_i) part of complex dielectric constant, with the incident wavelength. (d) the variation of n^2 with λ^2 for 1 wt% of Fe_2O_3-rGO doped in PVA.

part (ε_i) produces the complex dielectric function (ε^*) where $\varepsilon^* = \varepsilon_r + i\varepsilon_i$ [68] The dissipative rate of electromagnetic wave propagation in the medium is due to the imaginary part. However, the real portion of the dielectric constant is proportional to the dispersion, which depends primarily on the motion of electrons in the optical medium as light travels. The real and imaginary parts of the complex dielectric function rely on the refractive index (n), and extinction coefficient (k) according to the following relations [44, 48]:

$$\varepsilon_r = n^2 - k^2, \ \varepsilon_i = 2nk \tag{18}$$

For all the samples being examined, figures 8(b) and (c) illustrate the dependence of ε_i and ε_r on the incident wavelength, respectively. Interactions between the incident photon and free electrons in the different nanocomposites can explain the wavelength dependence of the real and imaginary parts of the dielectric constant at $\lambda < 750$ nm [69]. On the other hand, the values of ε_r become wavelength independent at higher wavelengths ($\lambda > 750$ nm) due to the incapability of the molecules of the samples to follow the fluctuations of the incident field [70]. It can be understood from the behavior of ε_i that the optical loss becomes higher at low wavelength compared to that at high wavelength. As the dielectric constants are dependent on the attenuation coefficient and refractive index, increasing the doped Fe_2O_3-rGO NPs in PVA increased the dielectric constants, including ε_i, and ε_r. This behavior was identical to that observed in figures 7(a) and (b) for the attenuation coefficient and refractive index, respectively.

3.3.6. High-frequency dielectric constant (ε_∞), and the ratio of (N_{opt}/m^*)

The high-frequency dielectric constant (ε_∞) and charge carrier concentration to effective mass ratio (N_{opt}/m^*) were determined by factoring in the influence of free carriers and dispersion vibration modes using the following relation [71]:

$$n^2 = \varepsilon_\infty - \frac{1}{4\pi^2\varepsilon_o}\left(\frac{e^2}{c^2}\right)\left(\frac{N_{opt}}{m^*}\right)\lambda^2 \tag{19}$$

Where ε_o is the free space permittivity, $N_{opt}$is the number of the carrier concentrations, m^* is the effective mass of the charge carriers, and e is the electronic charge. Plotting the square of the refractive index (n^2) versus the square of wavelength (λ^2) for 1 wt% of Fe_2O_3-rGO NPs doped in PVA, as an example for the others, is depicted in figure 8(d). The values of ε_∞ deduced from extrapolation of the linear portion of this plot, and the ratio of (N_{opt}/m^*) obtained from the slope were listed in table 3. Shen *et al* [41] determined the effective mass of the charge carriers (m^*, which equals the production of 0.44 times m_o), which was used to calculate the exact values of the charge carrier concentrations (N_{opt}), for all the examined samples. Table 3 shows that increasing the content of

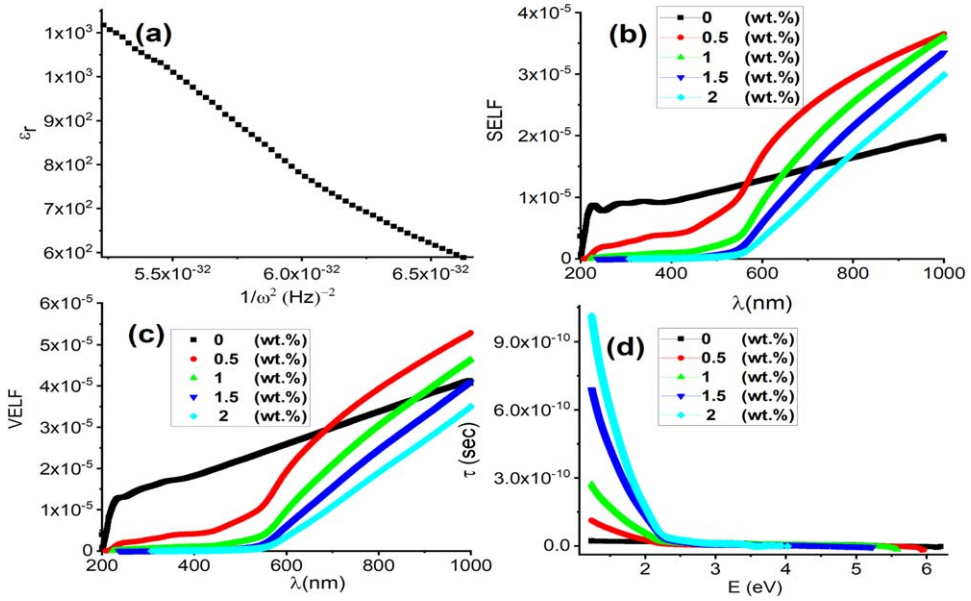

Figure 9. (d) variation of ε_r with $1/\omega^2$ for 2 wt% of Fe_2O_3-rGO NPs doped in PVA. For the different concentrations of Fe_2O_3-rGO NPs doped in PVA, plotting (b) SELF with the incident wavelength, (c) VELF with the incident wavelength, and (d) relaxation time (τ), with the incident photon energy.

Table 3. Ratio of (N_{opt}/m^*), high frequency dielectric constant (ε_∞), optical charge carriers ($N_{opt.}$), and plasma frequency (ω_P), for the different nanocomposites.

Fe_2O_3 - rGO NPs doped in PVA (wt%)	(N_{opt}/m^*) x10^{60} $(kg.m^3)^{-1}$	ε_∞ from equation (15)	$N_{opt.}$ x10^{30} (m^{-3})	ε_∞ from equation (16)	ω_p x10^{16} Hz
0	0.005	5.096	0.002	5.339	0.91
0.5	0.314	95.17	0.126	87.65	2.79
1	1.719	444.1	0.689	438.4	6.98
1.5	6.878	1597	2.757	1550	13.8
2	14.35	3282	5.755	3201	20.0

the doped Fe_2O_3 - rGO NPs in the host matrix resulted in an improvement in the values of ε_∞, N_{opt}, and the ratio of (N_{opt}/m^*) for all nanocomposites.

3.3.7. Plasma frequency and high-frequency dielectric constant (ε_∞)

It's worth noting that at the transparency range when the electron damping parameter (γ) is less than ω, the plasma frequency (ω_P), the real part of the dielectric constant (ε_r), and the high-frequency dielectric constant (ε_∞) are all related to each other as following [72]:

$$\varepsilon_r = \varepsilon_\infty - \frac{\omega_p^2}{\omega^2}, \quad \omega_p^2 = \frac{Ne^2}{\varepsilon_o\, m^*} \tag{20}$$

Figure 9(a) shows the variation of the real part of the dielectric constant (ε_r) with ω^{-2}, for 2 wt% of Fe_2O_3-rGO NPs doped in PVA, as an example for the other studied samples. The values of ω_p^2, and ε_∞ has given from the slope of the straight part of the plot in Figure 9(a), and the intercept, respectively. Table 3 shows the dependence of ω_p, and ε_∞on the doped amount of Fe_2O_3-rGO NPs in PVA. The values of ε_∞ deduced from equation (15) (5.096, 95.17, 444.1, 1597, and 3282) and those calculated from equation (16) (5.339, 87.65, 438.4, 1550, and 3201) corresponding to 0 wt%, 0.5 wt%, 1 wt%, 1.5 wt%, and 2 wt% of Fe_2O_3-rGO NPs doped in PVA, are remarkably close.

3.3.8. Energy loss function

It is interesting to know that electrons lose energy as they speed through a material because plasma oscillations in the conduction sea are excited [73]. The functions of volume energy loss (VELF) and surface energy loss (SELF) define the probability that fast electrons will undergo energy loss during their travels within and on the surface of the material, respectively [74]. Real (ε_r) and the imaginary (ε_i) parts of the dielectric constant were utilized to

calculate the values of (*VELF*) and (*SELF*) as the following [75]:

$$SELF = \frac{\varepsilon_i}{(\varepsilon_r + 1)^2 + \varepsilon_i^2} \tag{21}$$

$$VELF = \frac{\varepsilon_i}{\varepsilon_r^2 + \varepsilon_i^2} \tag{22}$$

For all the studied nanocomposites, the dependence of *SELF* and *VELF* on incident wavelength are shown in Figures 9(b) and (c), respectively. Increasing the content of the doped nanofillers in PVA resulted in lowering the surface and volume energy loss.

3.3.9. Dielectric relaxation time

The duration of time that it takes for the electric charges in semiconducting materials to be neutralized during conduction is measured by the dielectric relaxation time (τ). The dielectric relaxation time (τ) is extraordinarily small for metals but is regarded as large for insulators and small for semiconductors. The dielectric relaxation time (τ) was determined according to the following relation [76]:

$$\tau = (\varepsilon_\infty - \varepsilon_r)/\omega\varepsilon_i \tag{23}$$

Figure 9(d) reveals the variation of the dielectric relaxation time (τ) with the incident photon energy for all samples under investigation. Low energy region (E < 2.4 eV) showed dielectric relaxation time- energy dependent behavior, whereas the high energy region (E > 2.4 eV) displayed dielectric relaxation time- energy independent behavior. Also, the dielectric relaxation time (τ) mainly relies on the content of the doped Fe_2O_3-rGO NPs in PVA.

3.3.10. Nonlinear optical parameters

Miller's empirical rule was used to calculate the first-ordered nonlinear susceptibility ($\chi^{(1)}$) and the third-ordered nonlinear susceptibility ($\chi^{(3)}$) by using the calculated values of the average refractive index ($n_{average}$), as follows [77]:

$$\chi^{(1)} = \frac{(-1 + n_{average}^2)}{4\pi} \tag{24}$$

$$\chi^{(3)} = 1.7 \times 10^{-10} [\chi^{(1)}]^4 \tag{25}$$

Figure 10(a) illustrates the plotting of $\chi^{(1)}$ with the different contents of Fe_2O_3-rGO NPs doped in PVA. The best fit for the correlation between $\chi^{(1)}$ and the different contents of Fe_2O_3-rGO NPs is given by the following polynomial equation:

$$Y = A + B_1X + B_2 X^2 \tag{26}$$

Where Y is $\chi^{(1)}$, and the amount of Fe_2O_3-rGO NPs doped in PVA is given by X, A is 0.29, B_1 is 0.05, and B_{12} is 0.01.

Figure 10(b) displays the variation of $\chi^{(3)}$ with the amount of Fe_2O_3-rGO NPs doped in PVA. The following polynomial equation gives the best fit for the relationship between $\chi^{(3)}$, and the amount of Fe_2O_3-rGO NPs doped in PVA:

$$Y = A + B_1X + B_2 X^2 \tag{27}$$

Where Y defines $\chi^{(3)}$, and the amount of Fe_2O_3-rGO NPs doped in PVA is given by X, A is 1.4×10^{-12}, B_1 is 2.6×10^{-13}, and B_2 is 1.26×10^{-12}.

The nonlinear refractive index (n_2) was determined by using the following expression for all the examined samples [77]:

$$n_2 = \frac{12\pi\chi^{(3)}}{n_o} \tag{28}$$

Figure 10(c) depicts how the amount of Fe_2O_3-rGO NPs doped in PVA affects the nonlinear refractive index (n_2) of the various samples. The following polynomial equation provides the best description of the data in figure 10(c):

$$Y = A + B_1X + B_2 X^2 \tag{29}$$

Where X describes the amount of Fe_2O_3-rGO NPs doped in PVA, and n_2 is given by Y, A is 2.4×10^{-11}, B_1 is 6.6×10^{-12}, and B_2 is 1.6×10^{-11}. The values of $\chi^{(1)}$, $\chi^{(3)}$, and n_2 were increased by increasing the doped amount of Fe_2O_3-rGO NPs in PVA.

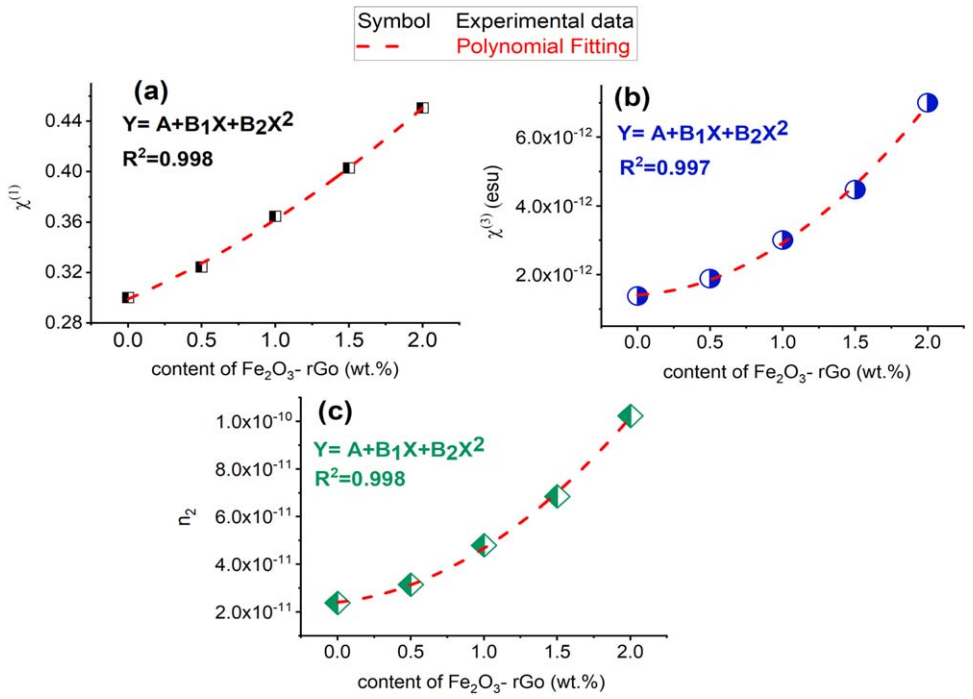

Figure 10. Plotting (a) $\chi^{(1)}$, (b) $\chi^{(3)}$, and (c) n_2 with the content of Fe_2O_3-rGO (wt%) doped in PVA.

4. Conclusion

Fe_2O_3-rGO-PVA films have been prepared via the casting method. The structure and optical properties of the PVA matrix have been affected by adding Fe_2O_3-rGO NPs. The degree of crystallinity of the polymer films was decreased with the addition of the Fe_2O_3-rGO NPs. The morphological analysis shows agglomerations in the PVA matrix with increasing Fe_2O_3-rGO NPs concentrations. The transparency of the polymer film decreases with the increase in Fe_2O_3-rGO NPs concentration. In addition, the Fe_2O_3-rGO NPs additive to the polymer matrix causes the film's transparency in the UV region to vanish, which makes the present polymer films a potential candidate for the UV shielding application. The skin depth of the nanocomposites was decreased with increasing Fe_2O_3-rGO NPs in the host matrix due to increasing the absorption and reducing the transparency. The additives of Fe_2O_3-rGO NPs to the PVA matrix can increase the conjugation in the monomer unit of the host matrix. The extinction coefficient was found to increase with increasing the wavelength of the incident photons (in the visible region), whereas this behavior disappeared upon introducing Fe_2O_3-rGO NPs to the matrix. The optical band gap was found to decrease from 5.956 eV for pure PVA film to 3.076 eV for 2.0 wt% Fe_2O_3-rGO NPs in PVA film. Moreover, the band tail width was found to increase with the increase in Fe_2O_3-rGO NPs in the PVA matrix, indicating the rise in polymer disordering and the decrease in the optical band gap. The values of $\chi^{(1)}$, $\chi^{(3)}$, and n_2 were increased by increasing the doped amount of Fe_2O_3-rGO NPs in PVA.

Acknowledgments

The authors would like to thank the Ural Center for Shared Use 'Modern nanotechnology' Ural Federal University (Reg.№ 2968), which is supported by the Ministry of Science and Higher Education RF (Project № 075-15-2021-677), for using the equipment.

Data availability statement

All data that support the findings of this study are included within the articl. The data that support the findings of this study are available upon reasonable request from the authors.

ORCID iDs

R M Ahmed https://orcid.org/0000-0002-2209-2503
T S Soliman https://orcid.org/0000-0001-7372-4761
S A Vshivkov https://orcid.org/0000-0003-1150-4960

References

[1] Ebnalwaled A A and Thabet A 2016 Controlling the optical constants of PVC nanocomposite films for optoelectronic applications *Synth. Met.* **220** 374–83
[2] Abdullah O G, Aziz S B, Omer K M and Salih Y M 2015 Reducing the optical band gap of polyvinyl alcohol (PVA) based nanocomposite *J. Mater. Sci., Mater. Electron.* **26** 5303–9
[3] Kuvshinova S A, Burmistrov V A, Koifman O I and Novikov I V 2015 PVC carbon nanostructure composite materials: approaches to their fabrication and properties *Nanotechnologies Russ.* **10** 1–12
[4] Ismail M S, Elamin A A, Abdel-Wahab F, Elbashar Y H and Mahasen M M 2022 Improving the refractive index by engineering PbS/PVA nano polymer composite for optoelectronic applications *Opt. Mater. (Amst).* **131** 112639
[5] Aziz S B, Hassan A Q, Mohammed S J, Karim W O, Kadir M F Z, Tajuddin H A and Chan N N M Y 2019 Structural and optical characteristics of PVA:C-dot composites: tuning the absorption of ultra violet (UV) region *Nanomaterials.* **9** 216
[6] Mohamed M B and Abdel-Kader M H 2020 Effect of annealed ZnS nanoparticles on the structural and optical properties of PVA polymer nanocomposite *Mater. Chem. Phys.* **241** 122285
[7] Selvi J, Parthasarathy V, Mahalakshmi S, Anbarasan R, Daramola M O and Senthil Kumar P 2020 Optical, electrical, mechanical, and thermal properties and non-isothermal decomposition behavior of poly(vinyl alcohol)–ZnO nanocomposites *Iran. Polym. J.* **29** 411–422
[8] Taha T A, Hendawy N, El-Rabaie S, Esmat A and El-Mansy M K 2019 Effect of NiO NPs doping on the structure and optical properties of PVC polymer films *Polym. Bull.* **76** 4769–84
[9] Ali H E, Abdel-Aziz M M, Khairy Y, Zahran H Y, Algarni H, Yahia I S, El-Shamy E F, Sayed M A, Maged F A and Sanaa M F 2021 Microstructure analysis and nonlinear/linear optical parameters of polymeric composite films based PVAL for wide optical applications *Phys. Scr.* **96** 115804
[10] Soliman T S, Vshivkov S A and Elkalashy S I 2020 Structural, thermal, and linear optical properties of SiO_2 nanoparticles dispersed in polyvinyl alcohol nanocomposite films *Polym. Compos.* **41** 3340–50
[11] Soliman T S, Rashad A M, Ali I A, Khater S I and Elkalashy S I 2020 Investigation of linear optical parameters and dielectric properties of polyvinyl Alcohol/ZnO nanocomposite films *Phys. Status Solidi Appl. Mater. Sci.* **217** 2000321
[12] Soliman T S and Abouhaswa A S 2020 Synthesis and structural of Cd0.5Zn0.5F2O4 nanoparticles and its influence on the structure and optical properties of polyvinyl alcohol films *J. Mater. Sci., Mater. Electron.* **31** 9666–74
[13] Soliman T S, Hessien M M and Elkalashy S I 2022 Structural, thermal, and optical properties of polyvinyl alcohol films doped with La2ZnOx nanoparticles *J. Non. Cryst. Solids.* **580** 121405
[14] Soliman T S, Vshivkov S A, Abdel-salam A I, Gomaa I and Khalid A 2023 Structural and optical parameters of polyvinyl alcohol fi lms reinforced with Mn_2O_3/reduced graphene oxide composite *Phys. Scr.* **98** 15832
[15] Badawi A, Alharthi S S, Althobaiti M G and Alharbi A N 2022 The effect of iron oxide content on the structural and optical parameters of polyvinyl alcohol/graphene nanocomposite films *J. Vinyl Addit. Technol.* **28** 235–46
[16] Badawi A and Alharthi S S 2022 The optical, electrical and mechanical performance of metal oxides incorporated PVA/rGO blend: effect of metal oxide type *Appl. Phys. A Mater. Sci. Process.* **128** 1–15
[17] Aslam M, Kalyar M A and Raza Z A 2017 Graphene oxides nanosheets mediation of poly(vinyl alcohol) films in tuning their structural and opto-mechanical attributes *J. Mater. Sci., Mater. Electron.* **28** 13401–13
[18] Periyasamy G, Patil I M, Kakade B, Veluswamy P, Archana J, Ikeda H and Annamalai K 2022 Reduced graphene oxide-wrapped α-Mn_2O_3/α-MnO_2 nanowires for electrocatalytic oxygen reduction in alkaline medium *J. Mater. Sci., Mater. Electron.* **33** 8644–54
[19] Li Z, Ji X, Han J, Hu Y and Guo R 2016 $NiCo_2S_4$ nanoparticles anchored on reduced graphene oxide sheets: In-situ synthesis and enhanced capacitive performance *J. Colloid Interface Sci.* **477** 46–53
[20] Abdel-Salam A I, Attia S Y, El-Hosiny F I, Sadek M A, Mohamed S G and Rashad M M 2022 Facile one-step hydrothermal method for $NiCo_2S_4$/rGO nanocomposite synthesis for efficient hybrid supercapacitor electrodes *Mater. Chem. Phys.* **277** 125554
[21] Li Y, Lv X, Lu J and Li J 2010 Preparation of SnO_2-nanocrystal/graphene-nanosheets composites and their lithium storage ability *J. Phys. Chem. C* **114** 21770–4
[22] Awad M M, Abdel-Salam A I, Elfeky S A, Rady H S, Hassanien A S, Mohamed M B and Elbashar Y H 2019 Tuning the optical properties of CdSe quantum dot using graphene nanocomposite *J. Opt.* **48** 616–25
[23] Hu Y, Guan C, Ke Q, Yow Z F, Cheng C and Wang J 2016 Hybrid Fe_2O_3 nanoparticle Clusters/rGO paper as an effective negative electrode for flexible supercapacitors *Chem. Mater.* **28** 7296–303
[24] Li H, Zhao Q, Li X, Zhu Z, Tade M and Liu S 2013 Fabrication, characterization, and photocatalytic property of α-Fe_2O_3/graphene *oxide composite, J. Nanoparticle Res.* **15** 1–11
[25] Zhang J, Jiang J and Zhao X S 2011 Synthesis and capacitive properties of manganese oxide nanosheets dispersed on functionalized graphene sheets *J. Phys. Chem. C* **115** 6448–54
[26] Han Y, Luo Z, Yuwen L, Tian J, Zhu X and Wang L 2013 Synthesis of silver nanoparticles on reduced graphene oxide under microwave irradiation with starch as an ideal reductant and stabilizer *Appl. Surf. Sci.* **266** 188–93
[27] Chapi S 2021 Influence of Co_2 + on the structure, conductivity, and electrochemical stability of poly(ethylene oxide)-based solid polymer electrolytes: energy storage devices *J. Electron. Mater.* **50** 1558–71
[28] Chapi S 2020 Optical, electrical and electrochemical properties of PCL5/ITO transparent conductive films deposited by spin-coating —materials for single-layer devices *J. Sci. Adv. Mater. Devices.* **5** 322–9
[29] Ali F M and Kershi R M 2020 Synthesis and characterization of La3 + ions incorporated (PVA/PVP) polymer composite films for optoelectronics devices *J. Mater. Sci. Mater. Electron.* **31** 2557–66
[30] Ali H E, Morad I, Algarni H, El-Desoky M M, Khairy Y, Zahran H Y and Yahia I S 2021 Structure analysis and nonlinear/linear optical properties of PVAOH/Si composites for low-cost optical technologies and limiting absorption *J. Mater. Sci. Mater. Electron.* **32** 4466–79

[31] Bao C, Guo Y, Song L and Hu Y 2011 Poly(vinyl alcohol) nanocomposites based on graphene and graphite oxide: a comparative investigation of property and mechanism *J. Mater. Chem.* **21** 13942–50

[32] Chapi S and Devendrappa H 2016 Optical, electrical, thermal and electrochemical studies of spin-coated polyblend-ZnO nanocomposites *J. Mater. Sci., Mater. Electron.* **27** 11974–85

[33] Ali F M, Yahia I S and Sayed M A 2019 Synthesis and optimization of a novel polymer: dye composite (PVA:MV-6B) films for band-stop optical filters *Optik (Stuttg).* **192** 162902

[34] Alghunaim N S 2016 Optimization and spectroscopic studies on carbon nanotubes/PVA nanocomposites *Results Phys.* **6** 456–60

[35] Rajeswari N, Selvasekarapandian S, Karthikeyan S, Prabu M, Hirankumar G, Nithya H and Sanjeeviraja C 2011 Conductivity and dielectric properties of polyvinyl alcohol–polyvinylpyrrolidone poly blend film using non-aqueous medium *J. Non. Cryst. Solids.* **357** 3751–6

[36] Mallakpour S and Khani Z 2018 Fabrication of poly(vinyl alcohol) nanocomposites having different contents of modified SiO_2 by vitamin B_1 as biosafe and novel coupling agent to improve mechanical and thermal properties *Polym. Compos.* **39** E1589–97

[37] El Sayed A M and Morsi W M 2014 α-Fe_2O_3/(PVA + PEG) nanocomposite films; Synthesis *optical, and dielectric characterizations, J. Mater. Sci.* **49** 5378–87

[38] Badawi A, Ahmed E M, Mostafa N Y, Abdel-Wahab F and Alomairy S E 2017 Enhancement of the optical and mechanical properties of chitosan using Fe2O3 nanoparticles *J. Mater. Sci., Mater. Electron.* **28** 10877–84

[39] Ahmed R M, Ibrahim A A and El-Said E A 2020 Enhancing the optical properties of polyvinyl alcohol by blending it with polyethylene glycol *Acta Phys. Pol. A* **137** 317–23

[40] Escobar-Alarcón L, Arrieta A, Camps E, Muhl S, Rodil S and Vigueras-Santiago E 2007 An alternative procedure for the determination of the optical band gap and thickness of amorphous carbon nitride thin films *Appl. Surf. Sci.* **254** 412–5

[41] Souri D and Shomalian K 2009 Band gap determination by absorption spectrum fitting method (ASF) and structural properties of different compositions of (60−x) V2O5–40TeO2–xSb2O3 glasses *J. Non. Cryst. Solids.* **355** 1597–601

[42] Peña-Flores J I, Palomec-Garfias A F, Márquez-Beltrán C, Sánchez-Mora E, Gómez-Barojas E and Pérez-Rodríguez F 2014 Fe effect on the optical properties of TiO2:Fe_2O_3 nanostructured composites supported on SiO_2 microsphere assemblies *Nanoscale Res. Lett.* **9** 1–7

[43] Abdel-salam A I, Gomaa I, Khalid A and Soliman T S 2022 Investigation of raman spectrum , structural , morphological , and optical features of Fe_2O_3 and Fe_2O_3/reduced graphene oxide hybrid nanocomposites *Phys. Scr.* **97** 125807

[44] Abdullah O G, Aziz S B, Omer K M and Salih Y M 2015 Reducing the optical band gap of polyvinyl alcohol (PVA) based nanocomposite *J. Mater. Sci., Mater. Electron.* **26** 5303–9

[45] Al-Hosiny N M, Abdallah S, Moussa M A A and Badawi A 2013 Optical, thermophysical and electrical characterization of PMMA (CdSe QDs) composite films *J. Polym. Res.* **20** 76

[46] Tauc J 1970 Absorption edge and internal electric fields in amorphous semiconductors *Mater. Res. Bull.* **5** 721–9

[47] Souri D, Mohammadi M and Zaliani H 2014 Effect of antimony on the optical and physical properties of Sb-V_2O_5-TeO_2 glasses *Electron. Mater. Lett.* **10** 1103–8

[48] Aslam M, Kalyar M A and Raza Z A 2017 Graphene oxides nanosheets mediation of poly(vinyl alcohol) films in tuning their structural and opto-mechanical attributes *J. Mater. Sci., Mater. Electron.* **28** 13401–13

[49] Aslam M, Kalyar M A and Raza Z A 2017 Fabrication of reduced graphene oxide nanosheets doped PVA composite films for tailoring their opto-mechanical properties *Appl. Phys. A Mater. Sci. Process.* **123** 1–12

[50] Saha V C, Sabuj M M A, Shams P, Rahman S, Qadir M R, Islam M R and Gulshan F 2018 Synthesis and characterization of reduced graphene oxide reinforced polymer matrix composite *IOP Conf. Ser.: Mater. Sci. Eng.* **438** 012008

[51] Raja V, Sarma A K and Rao V V R N 2003 Optical properties of pure and doped PMMA-CO-P4VPNO polymer films *Mater. Lett.* **57** 4678–83

[52] Al-Bataineh Q M, Alsaad A M, Ahmad A A and Telfah A 2020 A novel optical model of the experimental transmission spectra of nanocomposite PVC-PS hybrid thin films doped with silica nanoparticles *Heliyon.* **6** e04177

[53] Fink D *et al* 1995 Carbonaceous clusters in irradiated polymers as revealed by UV–vis spectrometry *Radiat. Eff. Defects Solids* **133** 193–208

[54] Ahmed R M 2014 Optical properties and structure of cobalt chloride doped PVA and its blend with PVP *Int. J. Mod. Phys. B* **28** 1450036

[55] ISO - ISO/CIE 10526:1999 - CIE standard illuminants for colorimetry, (n.d.) (https://iso.org/standard/30604.html) accessed December 28, 2022

[56] ISO - ISO 9050:2003 - Glass in building Determination of light transmittance, solar direct transmittance, total solar energy transmittance, ultraviolet transmittance and related glazing factors, (n.d.) (https://iso.org/standard/35062.html) accessed December 28, 2022

[57] Jelle B P, Gustavsen A, Nilsen T N and Jacobsen T 2007 Solar material protection factor (SMPF) and solar skin protection factor (SSPF) for window panes and other glass structures in buildings *Sol. Energy Mater. Sol. Cells* **91** 342–54

[58] ISO/CIE 10527:1991 *CIE standard colorimetric observers, (n.d.).* (https://infostore.saiglobal.com/en-au/standards/iso-cie-10527-1991-591732_saig_iso_iso_1355406/) accessed March 1, 2023

[59] B.S. Institution, ISO 9845-1 Solar energy — Reference solar spectral irradiance at the ground at different receiving conditions — Part 1: Direct normal and hemispherical solar irradiance for air mass 1, 5 part 1, 2021 (https://iso.org/obp/ui/#iso:std:iso:9845:−1:ed-2:v1:en) (accessed December 28, 2022)

[60] Ahmed R M 2009 Optical study on poly(methyl methacrylate)/poly(vinyl acetate) blends *Int. J. Photoenergy* **2009** 150389

[61] Ahmed R M, Ibrahiem A A and El-Said E A 2020 Effect of cobalt chloride as filler and PVP on the optical properties of PVA/PEG/PVP blends *Opt. Spectrosc.* **128** 642–55

[62] Nurhayati T, Iskandar F and Abdullah M 2013 Khairurrijal, syntheses of hematite (α-Fe2O3) nanoparticles using microwave-assisted calcination method *Mater. Sci. Forum* **737** 197–203

[63] Moss T S 1985 Relations between the refractive index and energy gap of semiconductors *Phys. Status Solidi* **131** 415–27

[64] Anani M, Mathieu C, Lebid S, Amar Y, Chama Z and Abid H 2008 Model for calculating the refractive index of a III-V semiconductor *Comput. Mater. Sci.* **41** 570–5

[65] Reddy R R and Ahammed Y N 1995 A study on the moss relation *Infrared Phys. Technol.* **36** 825–30

[66] Ravindra N M, Auluck S and Srivastava V K 1979 On the penn gap in semiconductors *Phys. Status Solidi* **93** K155–60

[67] Ahmed R M, Taha T A and Ezz-Eldin F M 2021 Investigation of Sm2O3 effect on opto-electrical parameters and dielectric properties of some fluorophosphate glasses *J. Mater. Sci., Mater. Electron.* **32** 28919–34

[68] Abdel-Salam A I, Khalid A, Awad M M, Hussein Y and Ahmed R M 2022 Investigating the impact of growth time of CdSe quantum dots on the structure and optical properties of its nanocomposites with SiO2 for improvement of optical devices *J. Alloys Compd.* **925** 166729

[69] Shehap A M and Akil D S 2016 Structural and optical properties of TiO2 nanoparticles/PVA for different composites thin films, *Int. J. NanoelectronMater.* **9** 17–36
[70] Hecht E Optics 4th edition (San Francisco, San Francisco: Addison Wesley2002) (https://academia.edu/44357906/Optics_hecht_and_zajac_4th_ed) accessed December 28, 2022
[71] Zemel J N, Jensen J D and Schoolar R B 1965 Electrical and optical properties of epitaxial films of PbS, PbSe, PbTe, and SnTe *Phys. Rev.* **140** A330
[72] El-Nahass M M, Sallam M M, Rahman S A and Ibrahim E M 2006 Optical, electrical conduction and dielectric properties of $TlGaSe_2$ layered single crystal *Solid State Sci.* **8** 488–99
[73] Pines D and Bohm D 1952 A collective description of electron interactions: ii. collective vs individual particle aspects of the interactions *Phys. Rev.* **85** 338
[74] El-Nahass MM, Soliman HS, Hendi AA and El-Gamdy S 2011 Effect of Annealing on The Structural and Optical Properties of Tertracyanoquinodimethane Thin Films *Aust. J. Basic Appl. Sci.* **5** 145–56
[75] Ritchie R H 1957 Plasma Losses by fast electrons in thin films *Phys. Rev.* **106** 874
[76] El-Nahass M M, Farag A A M, Ibrahim E M and Abd-El-Rahman S 2004 Structural, optical and electrical properties of thermally evaporated Ag2S thin films *Vacuum* **72** 453–60
[77] Yadav P and Sharma A 2015 Investigation of optical nonlinearities in Bi-doped Se-Te chalcogenide thin films *J. Electron. Mater.* **44** 916–21